RESEARCH PAPER

Analysis of heat transfer and material flow in reverse dual-rotation friction stir welding

L. Shi · C. S. Wu · H. J. Liu

Abstract Reverse dual-rotation friction stir welding (RDR-FSW) is a novel variant of conventional FSW process. The key feature is that the tool pin and the assisted shoulder rotate reversely and independently during the process; thus, it has great potential to improve the weld quality and lower the welding loads through adjusting the rotating speeds of the tool pin and the assisted shoulder independently. In this study, a 3D model of RDR-FSW process is developed to conduct the numerical simulation of heat generation, material flow, and temperature profile during the process. Heat generated due to plastic deformation and friction at the tool-workpiece contact interfaces are both considered. Streamlines show that there are two material flows with reverse direction, which is beneficial to the uniformity of both the temperature and the microstructure at the advancing side and retreating side. The simulation results show that rotating speeds of the assisted shoulder and the tool pin have great effects on the shape and size of the thermo-mechanically affected zone (TMAZ). The calculated peak temperatures at typical locations match with the experimentally measured ones. It lays solid foundation to optimize the process parameters in RDR-FSW.

L. Shi · C. S. Wu (✉)
MOE Key Lab for Liquid-solid Structure Evolution and Materials Processing, and Institute of Materials Joining, Shandong University, Jinan 250061, China
e-mail: wucs@sdu.edu.cn

C. S. Wu · H. J. Liu
State Key Lab of Advanced Welding and Joining, Harbin Institute of Technology, Harbin 150001, China

1 Introduction

Friction stir welding (FSW) is a solid-state, hot-shear joining process. This process can be used to join high-strength aluminum alloys and other metallic alloys that are hard to weld by fusion welding [1]. In FSW, a non-consumable rotating tool with a specially designed pin and shoulder is inserted into the abutting edges of the workpieces to be welded, and traversed along the line of joint. Heat generated by friction between the tool and the workpiece and plastic deformation of workpiece softens the material around the pin, and combination of tool rotation and translation leads to transportation of material from the front of the pin to the back of the pin where it is forged into a joint [1, 2].

However, in conventional FSW, some differences of heat transfer and material flow behavior occur between the advancing side and the retreating side due to the rotation and motion of the tool, leading to the corresponding differences of the microstructures and mechanical properties at both sides, which has negative influence on the performance of the welded structure [3, 4]. On the other hand, the relative high peripheral velocity at the outer edge of the shoulder might even lead to overheating or incipient melting along the shoulder edge on the weld surface, which has great deterioration on microstructures and mechanical properties of the joint, especially for joining thick plates, because usually the shoulder diameter is threefold to the plate thickness [5, 6].

To solve the problems mentioned above, Liu proposed the reverse dual-rotation FSW (RDR-FSW) as a variant technique [5, 7]. In RDR-FSW process, the tool pin and assisted shoulder are separately designed and manufactured so that they can rotate independently in reverse direction. Thus, the tool pin can rotate in a relatively high speed without a corresponding increase of the shoulder peripheral speed, so the tendency towards overheating or incipient melting can be reduced through optimizing rotation speeds of both the tool pin and

the assisted shoulder during welding thick plates. During the RDR-FSW process, the tool pin with sub-size concave shoulder rotates in counterclockwise direction. Thus, the torque exerted on the workpiece by the tool pin with sub-size concave shoulder is in positive z direction. However, the assisted shoulder rotates in clockwise direction which results in a torque exerted on the workpiece in negative z direction. As a result, the welding torque exerted on the workpiece by the tool pin can be partly offset by the reversely rotating assisted shoulder, so the total net torque exerted on the workpiece can be reduced and the welding loads can be lowered. Previous work has shown that there are two materials flows with reverse direction around the tool due to the tool pin and the assisted shoulder are separated and reversely rotated independently [8]. The temperature difference between advancing side (AS) and retreating side (RS) has been weakened in RDR-FSW compared to conventional FSW [9], and the mechanical properties of the weld joint can be improved by RDR-FSW process [5, 7]. However, independent rotation of the tool pin and the assisted shoulder increases the number of the process parameters and the complexity of the underlying physical mechanisms during the RDR-FSW process. To optimize the welding parameters, the effect of welding parameters on the temperature distribution and the size and shape of the weld joints need to be quantitatively analyzed. In this study, a computational fluid dynamics (CFD)-based model of RDR-FSW process is developed to analyze the heat generation, temperature profile, and material flow quantitatively during the RDR-FSW process. The effect of welding parameters on temperature distribution and the size and shape of the thermo-mechanically affected zone (TMAZ) are highlighted in this paper. It lays foundation for establishing the knowledge base and optimizing the process.

2 Formulation

The RDR-FSW tool system consists of two main parts: the tool pin with the sub-size concave shoulder and the assisted shoulder [5, 7]. During the welding process, the pin with the sub-size concave shoulder rotates with the main spindle of the FSW machine, while the assisted shoulder rotates independently and reversely driven by two servo motors. As shown in Fig. 1, the tool pin is mounted on the spindle of the FSW machine. Therefore, it rotates at the same rotation speed and in the same rotation direction as the spindle during the welding process. The assisted shoulder is machined on the bottom end cover, which is fixed on the middle cylinder through four bolts as shown in Fig. 1b. Through a deep groove ball bearing and a tapered roller bearing, the middle cylinder is assembled with the shaft which is fixed on the spindle of the conventional FSW machine. The assisted shoulder system is mounted on the supported frame for the servo motors. The supported

frame is installed on the fixed frame of the conventional FSW machine. Then, the assisted shoulder can penetrate into the workpiece as the spindle of the FSW machine is moved downward when the tool pin is plunging into the workpiece. In this way, the plunge force from the FSW machine is given to the assisted shoulder through the support frame for the servo motors. Thus, the axial pressure of the assisted shoulder is given to the workpiece. Detail description of the RDR-FSW system could be found in Ref [5] and Ref [7].

Figure 2 shows the geometric model in the simulation. In RDR-FSW, the AS is the half plate where the tangential direction of the rotating tool pin with the sub-size concave shoulder (not the assisted shoulder) is the same as the welding direction, and the other side is taken as the RS. The tilt angle of the tool and the concave of the sub-size concave shoulder are not considered. The RDR-FSW tool is not included in this geometric model but being treated as a rigid body. The 0.1-mm gap between the assisted shoulder and the sub-size concave shoulder is ignored. The dimensions of the tool are shown in Table 1. Only the quasi-steady-state welding period is dealt with in this study. During the welding period, the material near the tool is heated to a relatively high temperature, and only the plastic deformation is considered. The mass flow during RDR-FSW is treated as non-Newtonian, incompressible, single-phase viscoplastic material as in conventional FSW process [10, 11].

The conservation equations are as follows:

(1) The continuity equation for incompressible flow in index form is given by

$$\frac{\partial u_i}{\partial x_i} = 0 \tag{1}$$

where u is the velocity of material flow and index notation for $i=1$, 2, and 3 representing x, y, and z directions, respectively.

(2) The quasi-steady-state conservation of the momentum equation in index form can be written as follows:

$$\rho \frac{\partial u_i u_j}{\partial x_i} = -\frac{\partial p}{\partial x_j} + \frac{\partial}{\partial x_i}\left(\mu\frac{\partial u_j}{\partial x_i} + \mu\frac{\partial u_i}{\partial x_j}\right) - \rho U\frac{\partial u_j}{\partial x_j} \tag{2}$$

where ρ is the density which is taken as 2780 kg/m^3 for 2024 aluminum alloy, and its solidus temperature is taken as 815 K in this paper. U is the welding speed, p is the pressure, and μ is the non-Newtonian viscosity.
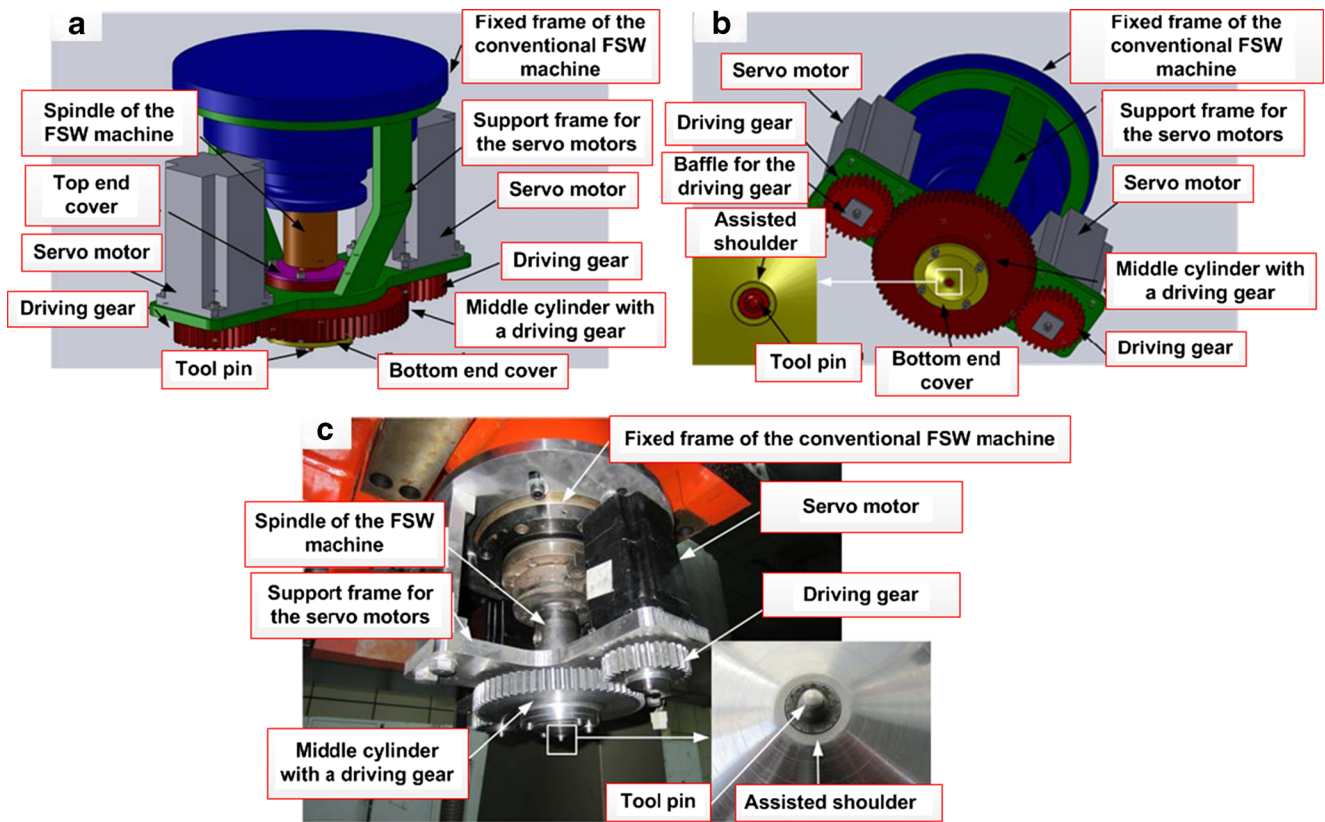
Fig. 1 Tool system for the RDR-FSW. **a** Schematic isometric view, **b** schematic bottom view, and **c** experimental set up photo

(3) The quasi-steady-state energy conservation equation can be written as follows:

$$\rho C_p \frac{\partial(u_i T)}{\partial x_i} = -\rho C_p U \frac{\partial T}{\partial x_1} + \frac{\partial}{\partial x_i}\left(k\frac{\partial T}{\partial x_i}\right) + S_v \qquad (3)$$

where k is the thermal conductivity, and C_p is the specific heat of the material. Both the thermal conductivity and specific heat of 2024 aluminum alloy are taken from Ref [12] as list in Table 2. T is the temperature, and S_v is the source term which represents the heat generation rate due to viscous
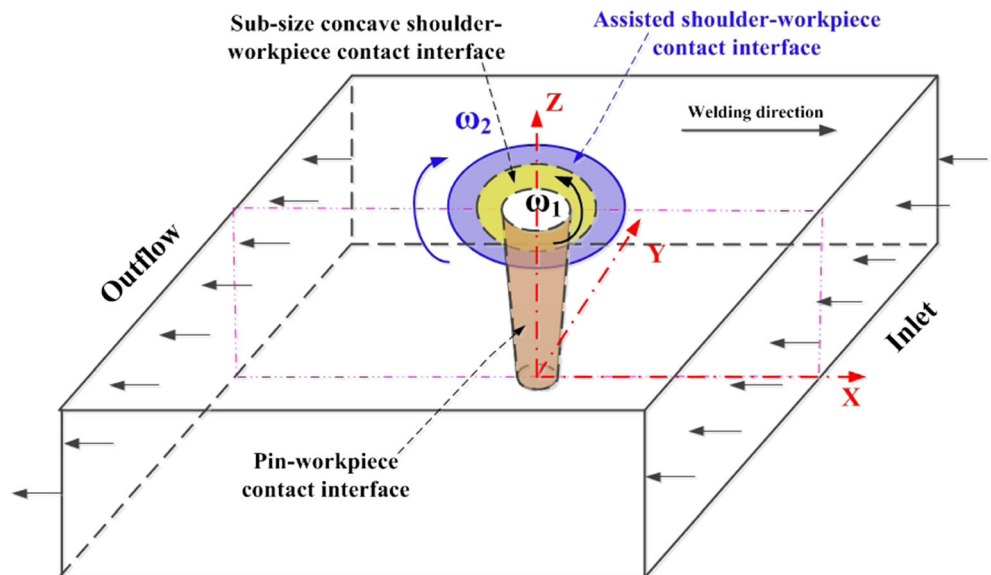
Fig. 2 Geometric model of RDR-FSW process

Table 1 Tool and workpiece dimensions for RDR-FSW

Items	RDR-FSW
Shoulder radius/mm	R_{out}=7.0 mm for assisted shoulder; R_{in}=5.0 mm for sub-size concave shoulder
Pin radius/mm	R_{po}=2.5 mm at the root; R_{pi}=2.0 mm at the tip
Pin length/mm	4.8 mm
Workpiece dimension	100 mm×100 mm×5 mm

dissipation in the workpiece away from the contact interfaces [10].

(4) The expression of viscosity used in this simulation is written as [12]

$$\mu = \frac{1}{3\varepsilon\alpha}\ln\left\{\left(\frac{Z}{A}\right)^{\frac{1}{n}} + \left[1 + \left(\frac{Z}{A}\right)^{\frac{2}{n}}\right]^{\frac{1}{2}}\right\} \qquad (4)$$

where Z is the Zenner-Hollomon parameter, $\dot{\varepsilon}$ is the effective strain rate, and α, A, and n are the material constants [13].

The total heat generation rate at the tool-workpiece contact interfaces could be calculated by taking into consideration both frictional heat and plastic deformation heat. The heat flux at the tool-workpiece contact interface under the assisted shoulder is expressed as follows [8]:

$$k\frac{\partial T}{\partial z} = f\left[\eta\delta\tau_c + (1-\delta)\mu_f P_2\right](\omega_2 r + U\sin\theta), \quad (R_{in} \le r \le R_{out}) \qquad (5)$$

where f is the percentage of the heat conducted into the workpiece according to the effusivity of the workpiece and tool material [11], since part of the total heat generated at the contact interfaces is conducted to the workpiece while the rest is conducted to the tool. η is the efficiency of plastic deformation work, τ_c is the shear yield stress [12], and δ is the sticking rate, which is selected as 0.25 by trial and error, since the calculated peak temperature at typical locations agree well with the corresponding experimentally measured ones when the sticking rate is equal to 0.25. And this value locates within the

experimental measured range (0.1–0.3) by Schmidt et al. [14] during conventional FSW of 2024 aluminum alloys. μ_f is the friction coefficient at the tool-workpiece contact interfaces as a function of local temperature which is obtained from Ref [15], P_2 is the axial pressure of assisted shoulder, ω_2 is the rotating speed of the assisted shoulder, r is the length between the elemental area and the tool axis, and θ is the angle between the welding direction and the r radius vector direction.

Similarly, the heat flux at the tool-workpiece contact interface under the sub-size concave shoulder and the bottom of the tool pin can be written as follows [10]:

$$k\frac{\partial T}{\partial z} = f\left[\eta\delta\tau_c + (1-\delta)\mu_f P_1\right](\omega_1 r - U\sin\theta), \qquad (6)$$
$$\left(R_{po} \le r < R_{in} \text{ or } 0 \le r \le R_{pi}\right)$$

where P_1 is the axial pressure of tool pin with sub-size concave shoulder, and ω_1 is the rotating speed of tool pin with sub-size concave shoulder.

In this study, the tool pin is a taper cylinder. At the side surface of the tool pin and the workpiece contact interface, the heat flux is given as follows [16]:

$$k\frac{\partial T}{\partial n} = f\left[\eta\delta\tau_c + (1-\delta)\mu_f \sigma_{yield}\right](\omega_1 r - U\sin\theta), \qquad (7)$$
$$\left(R_{pi} < r < R_{po}\right)$$

where σ_{yield} is the yield stress which lists in Table 3.

3 Results and discussion

Based on the numerical model, the heat generation at the tool-workpiece contact interfaces and the temperature distribution and plastic material flow in quasi-steady state are numerically simulated. The process parameters are listed in Table 4, and the axial pressure of the assisted shoulder and the tool pin is kept as a constant value of 29.5 MPa.

Figure 3 illustrates the heat generation rate at the tool-workpiece contact interface in RDR-FSW under the welding parameters of Test No. 2. Heat generation pattern is nearly symmetric about the tool axis. The peak heat generation rate locates at the outer diameter of the assisted shoulder due to its highest relative velocity between the tool-workpiece contact

Table 2 Specific heat capacity and thermal conductivity of 2024 aluminum alloy

Temperature (K)	290	373	473	573	673
Specific heat capacity (J·kg^{-1}·K^{-1})	864.0	921	1047	1130	1172
Thermal conductivity (W·m^{-1}·K^{-1})	120.0	134.4	151.2	172.2	176.4

Table 3 Yield stress of 2024 aluminum alloy

Temperature (K)	297	373	422	477	533	589	644
Yield stress (MPa)	345	331	310	138	62	41	28

Table 4 The process parameters in RDR-FSW (the assisted shoulder rotating in clockwise direction, while the pin rotating in counterclockwise direction in RDR-FSW)

Test No.	RDR-FSW		
	Welding speed (mm/min)	Rotating speed of assisted shoulder (rpm)	Rotating speed of pin (rpm)
1	100	−800	600
2	100	−800	800
3	100	−800	1000
4	100	−800	1200
5	100	−600	800
6	100	−1000	800
7	100	−1200	800
8	50	−800	800
9	150	−800	800
10	200	−800	800

interfaces. At the bottom of the tool pin, heat generation rate shows similar trends to the shoulder except of smaller magnitude due to relatively short diameter. However, the RDR-FSW process has great potential to obtain appropriate welding heat input through adjusting the rotating tool pin and assisted shoulder independently since the tool pin and assisted shoulder are separated. The tool pin can rotate in a relatively high rotation speed to soften the material near the tool pin, while the assisted shoulder can rotate in an appropriate matching rotation speed without a corresponding increase of the assisted shoulder peripheral speed to reduce the heat input at the shoulder edge during welding thick plates. Thus, the overheating or incipient melting at the shoulder edge in conventional FSW of thick plates can be avoided through optimizing rotation speeds of both the tool pin and the assisted shoulder. As a result, the weld quality can be improved.

Figures 4 and 5 depict the temperature field for different welding parameters at the total workpiece and at transverse cross section, respectively. The region where its peak temperature is higher than about 650 K in FSW of 2024 aluminum alloy would experience an overaging process with the dissolution of Guinier-Preston-Bagaryatsky (GPB) zones and solute clusters, as well as the formation and coarsening of S phases [17]. The dissolution of the GPB zones and solute clusters as well as the coarsening of S phases has great deterioration on microstructures and mechanical properties. Thus, the region of 650 K was selected as a case to analyze the effect of the welding parameter on the temperature distribution in this paper. The high temperature region (over 650 K) is enlarged as the rotating speed of the tool pin with sub-size concave shoulder or the assisted shoulder increases, but contracted as the welding speed goes up. The tool pin has dominant effect on the temperature field near the tool. With increasing the rotating speed of the tool pin, the temperature region of the same value is enlarged more than that with increasing the rotating speed of the assisted shoulder. This can be attributed to that the contact area between the tool pin (with sub-size shoulder) and the workpiece is nearly 1.7 times of the contact area between the assisted shoulder and the workpiece.

Figure 6 compares the calculated peak temperature and the measured ones at typical locations in $Z=3$ mm plane, i.e., at 2-mm depth from the top surface of the workpiece. The peak temperature at typical locations was measured by K-type thermal couples during the RDR-FSW process. In order to measure the peak temperature, little holes of 2-mm depth ($Z=3$ mm plane) were drilled from the top surface of the workpiece, and the K-type thermal couples were inserted into the little holes and joined at the hole bottom. It depicts that the calculated peak temperature matches well with the measured peak temperature.
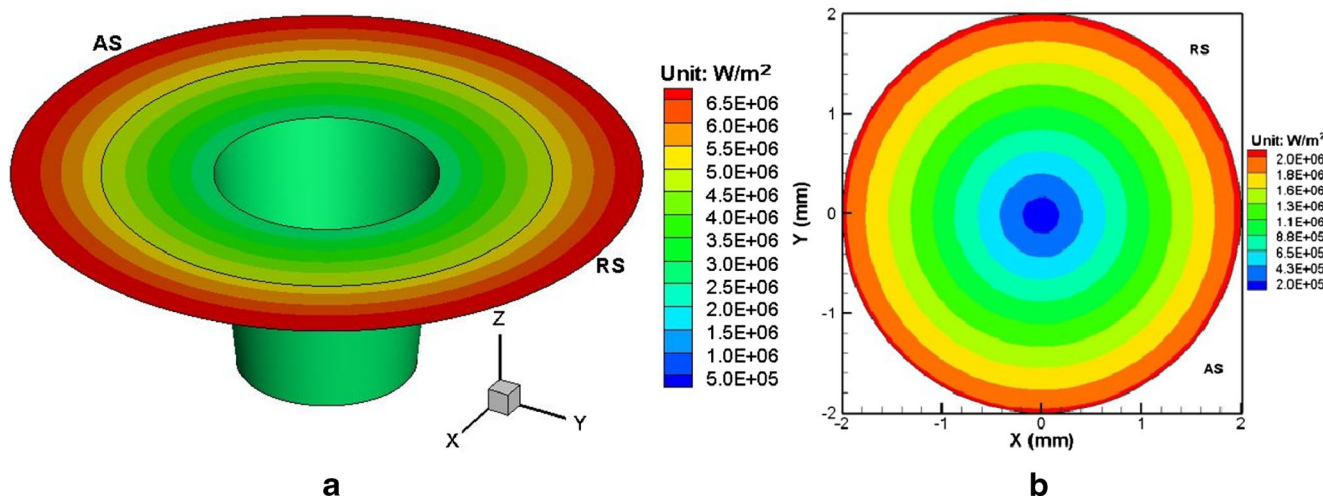

Fig. 3 Spatially variable heat flux at the tool-workpiece contact interface for Test No. 2 **a** at shoulder and the pin profile and **b** at the bottom of pin
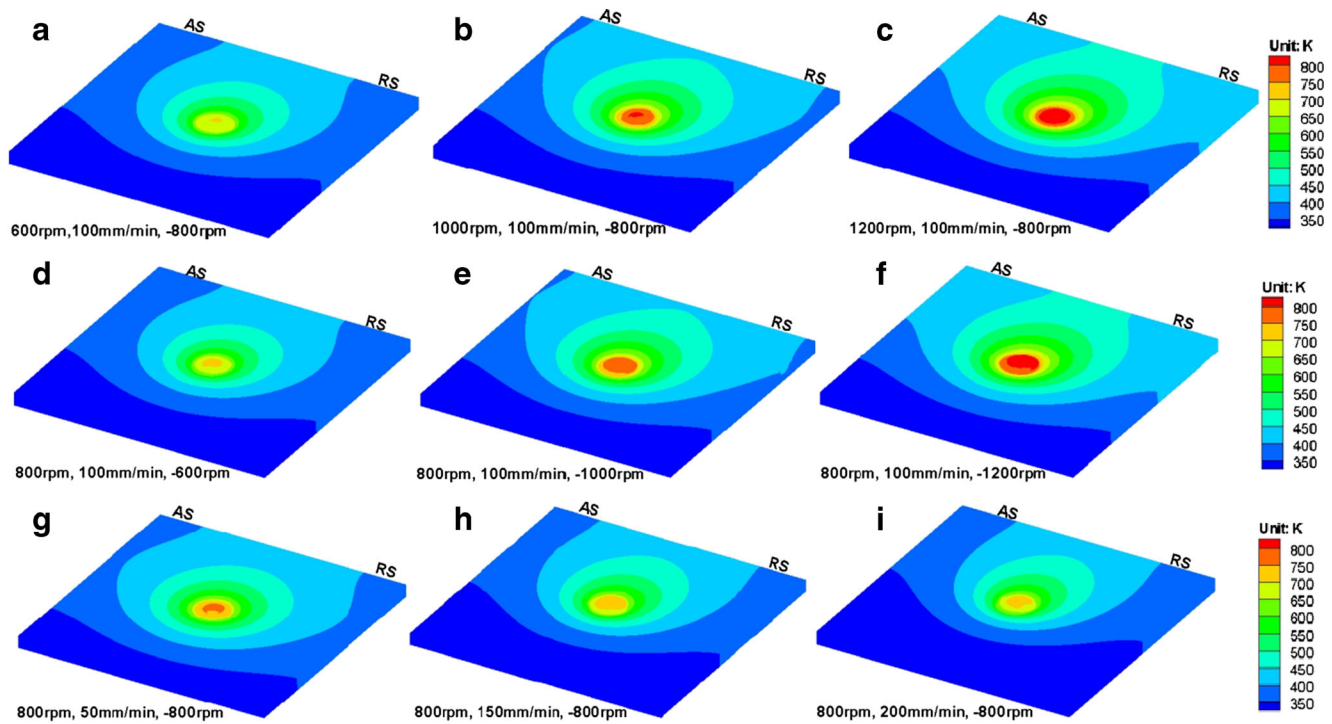
Fig. 4 Temperature field for different welding parameters. **a** Test No. 1, **b** Test No. 3, **c** Test No. 4, **d** Test No. 5, **e** Test No. 6, **f** Test No. 7, **g** Test No. 8, **h** Test No. 9, and **i** Test No. 10

Figure 7 depicts the calculated streamlines and velocity field near the tool at plane $Z=3.5$ mm for Test No. 3. Two reverse material flows could be clearly seen at this depth due to the tool pin and the assisted shoulder rotate in reverse direction during the RDR-FSW, which is beneficial to the uniformity of the temperature profile. The streamlines show that plastic material at AS flows in clockwise direction and passes through the tool at AS under the effect of the assisted shoulder.

However, plastic material at RS will firstly flow in clockwise direction, then changes its flow direction under the effect of the tool pin with sub-size concave shoulder, and passes the tool at RS. Two reverse material flows could be clearly seen near the tool. One is the counterclockwise material flow by the tool pin which leads to the temperature at AS being higher than that at RS because the relatively hot material at the rear of the tool is transported to the AS while the cold material in
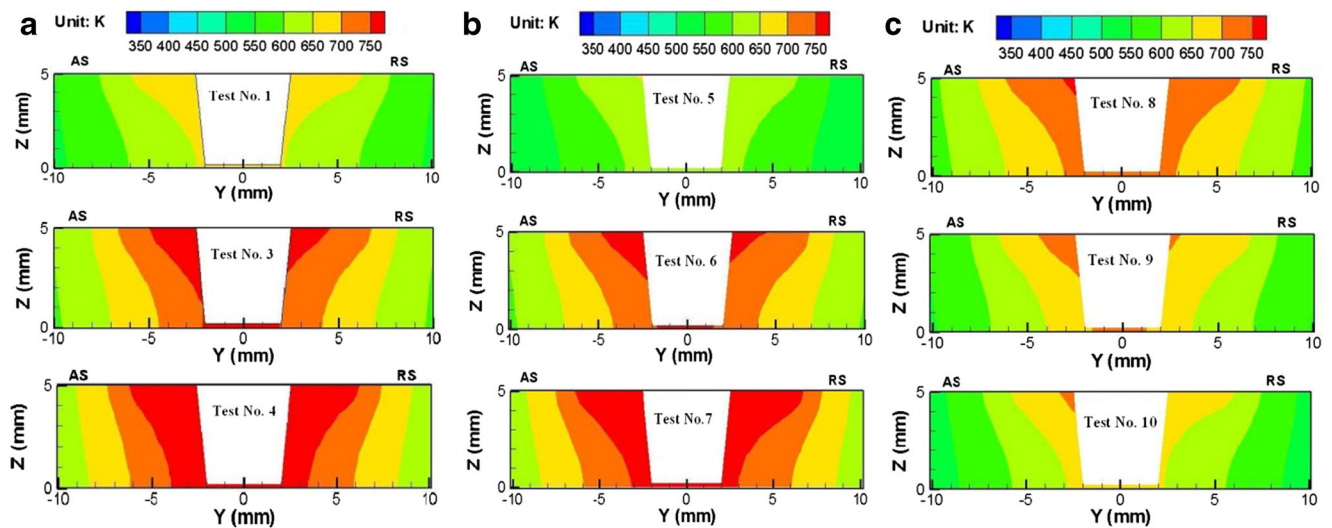

Fig. 5 Temperature field at transverse cross section. **a** Different rotating speed of the tool pin. **b** Different rotating speed of the assisted shoulder. **c** Different welding speed
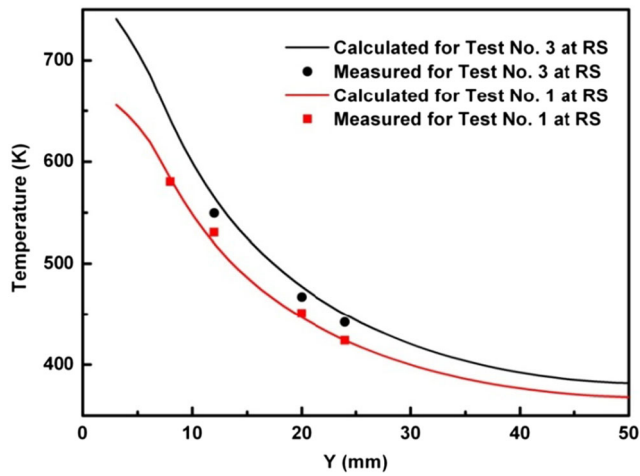
Fig. 6 Comparison between the calculated and the measured peak temperature (Z=3 mm plane)

generation rate on RS under the assisted shoulder. The higher heat generation rate on RS under the assisted shoulder can reduce the temperature difference caused by the higher heat generation rate on AS under the tool pin with sub-size concave shoulder. As a result, the temperature difference is further reduced and the uniformity of the temperature profile is further improved by the separated and reverse rotation tool pin and assisted shoulder in RDR-FSW.

Figure 8 shows the calculated magnitude of material flow velocity near the tool. The maximum velocity during RDR-FSW is about 0.14 m/s, which is about 25 % of the maximum tool velocity at the out diameter of the assisted shoulder. Although the assisted shoulder makes the diameter of the total shoulder diameter enlarged, it has little effect on the velocity of the material flow under the sub-size concave shoulder and near the tool pin due to the reverse rotating direction. The velocity around the tool pin is confined to a relatively small region. The region with the same velocity magnitude near the

front of the tool is transported to the RS, like that in conventional FSW process. The other one is the clockwise material flow by the assisted shoulder which leads to some of the relatively hot material at the rear of the tool being transported to the RS. Thus, the temperature difference between the AS and RS originated by the rotation of the tool pin can be reduced. Two reverse material flows are beneficial to the uniformity of the temperature profile. Furthermore, the higher relative velocity $(\omega r - U \sin\theta)$ on AS $(\sin\theta < 0)$ under the tool pin with sub-size concave shoulder leads to a higher heat generation rate on AS there. However, the higher relative velocity $(\omega r + U \sin\theta)$ on RS $(\sin\theta > 0)$ results in a higher heat
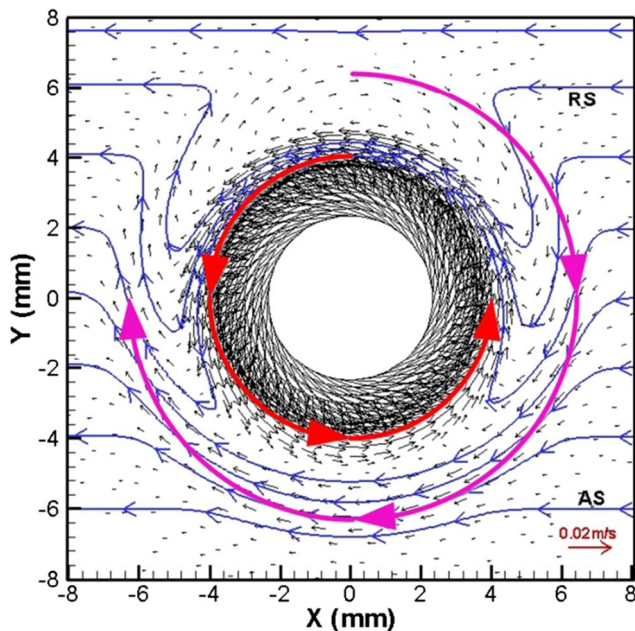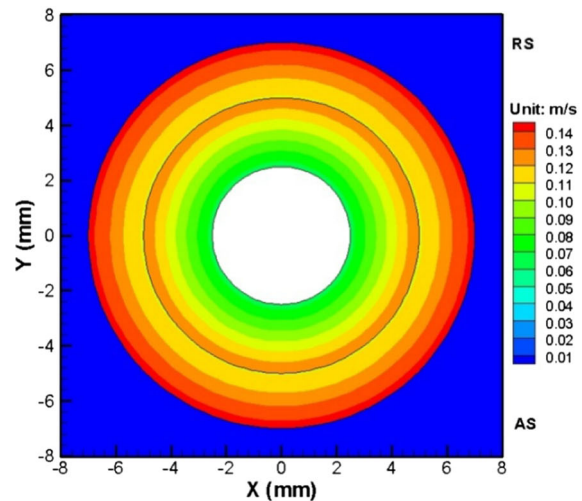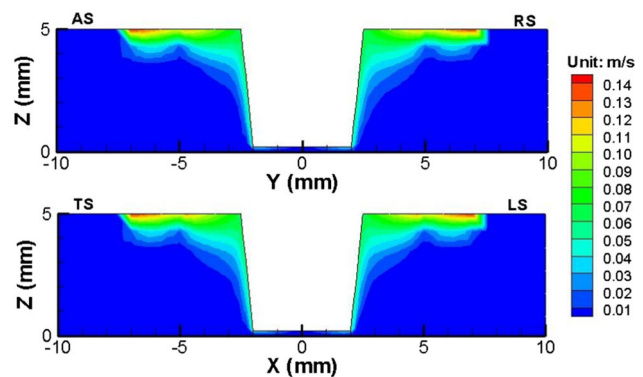

(a) Top of the workpiece

(b) Transverse section (top) and longitudinal section (bottom)

Fig. 8 Plot of material flow velocity magnitude near the tool (Test No. 3). **a** Top of the workpiece. **b** Transverse section (*top*) and longitudinal section (*bottom*)

Fig. 7 Calculated streamlines and velocity field near the tool at plane Z=3.5 mm (Test No. 3)

tool pin at the RS is larger than that at the AS since the bulk material flow by the tool pin is from RS as shown in Fig. 7. However, the flow region with the same velocity magnitude underneath the assisted shoulder at the AS is slightly larger than that at the RS as the bulk material flow by assisted shoulder is from AS. The material flow velocity magnitude shows similar trends at both leading side (LS) and trailing side (TS).

Figure 9 demonstrates the shape and size of TMAZ at transverse cross section, which are predicted by iso-viscosity line of 2.5×10^6 kg·m^{-1}·s^{-1}. Figure 9a shows that the size of

TMAZ under the assisted shoulder expands as the rotating speed of the assisted shoulder increases. That means the rotating speed of the assisted shoulder has great influence on the size of the whole TMAZ. Figure 9b shows that the size of TMAZ near the tool pin and under the sub-size concave shoulder increases as the rotating speed of the pin goes up. However, the size of TMAZ under the assisted shoulder makes no difference. From Fig. 9b, it could be found that the size of TMAZ at the advancing side increases faster than that at the retreating side as the rotating speed of the tool pin
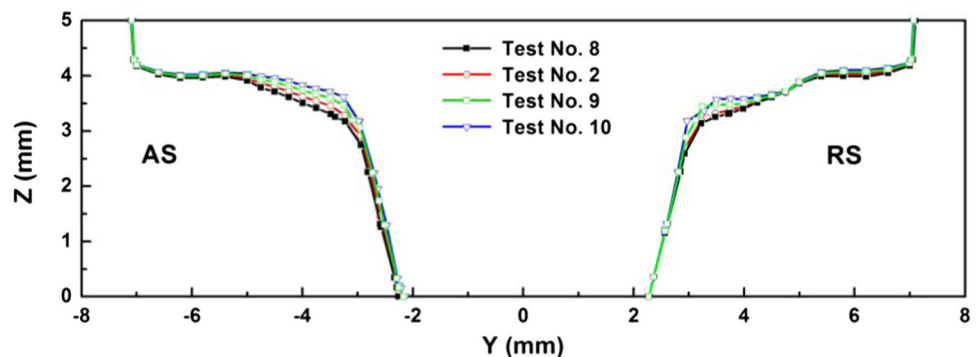

Fig. 9 The shape and size of TMAZ at transverse cross section. a Different rotating speed of the assisted shoulder. b Different rotating speed of the tool pin. c Different welding speed
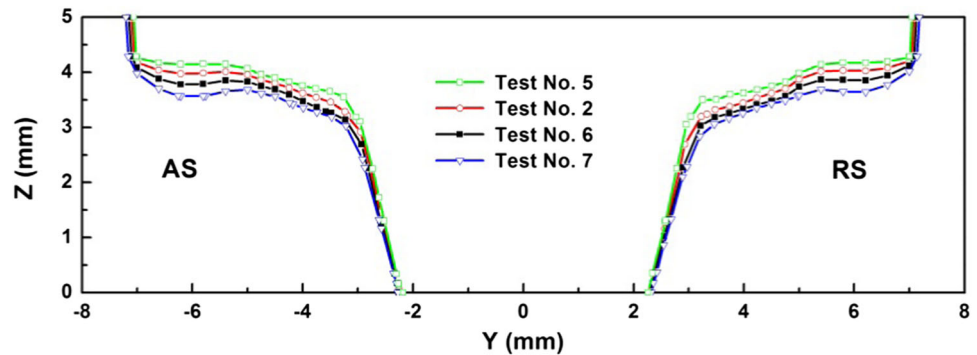
(a) Different rotating speed of the assisted shoulder
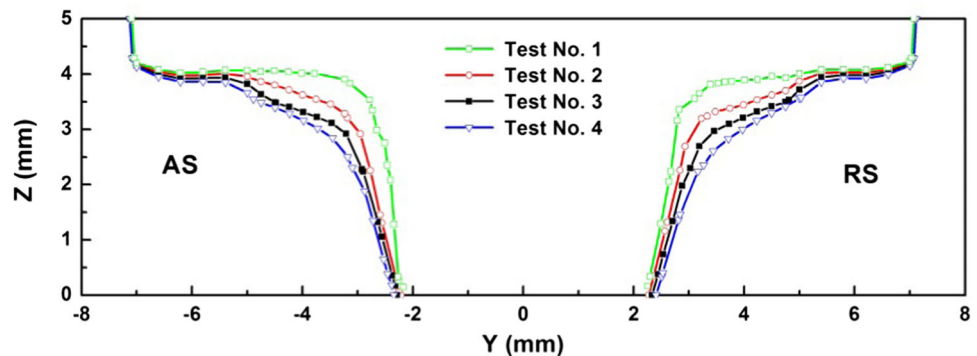
(b) Different rotating speed of the sub-size concave shoulder and the pin
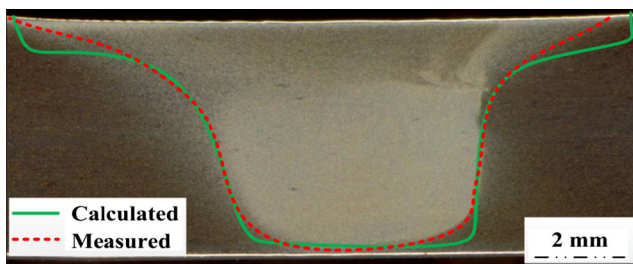
(c) Different welding speed

Fig. 10 The comparison of the calculated and measured boundary of TMAZ at transverse cross section (Test No. 2)

goes up. This may be because that the material flow at AS near the tool pin is assisted by the bulk material flow due to the assisted shoulder. When the rotating speed of the pin is lower, the difference of the TMAZ size between AS and RS is significant, but as the rotating speed of the pin increases, the difference gets weakened. It means that with increasing of the rotating speed of the pin with the sub-size concave shoulder, the symmetry of the TMAZ at AS and RS will be improved, which finally would increases the mechanical properties of the joints. Figure 9c shows that as the welding speed increases, the size of TMAZ will decrease slightly both under the shoulder and near the pin. Both the rotating speed of the pin and the welding speed have greater influence on the size of TMAZ at the advancing side than that at the retreating side.

Figure 10 shows the comparison of the calculated and measured boundary of TMAZ at transverse cross section for Test No. 2 in RDR-FSW process. The calculated boundary of TMAZ based on the iso-viscosity value of 2.5×10^6 kg·m^{-1}·s^{-1} is superimposed as a green line in the macrograph of the joint section. It shows that the experimental measured boundary of TMAZ is generally in agreement with the calculated one. It should be noted that there is some difference at the edge of the assisted shoulder because the effect of the flash near the edge of the shoulder has not been considered in this model which leads to a relatively larger calculated boundary of the TMAZ near the assisted shoulder edge.

4 Conclusions

(1) A CFD model is developed to quantitatively analyze the material flow and heat transfer during RDR-FSW process. The model can be used for predicting the heat generation and temperature profile in RDR-FSW. The calculated results agree with the experimentally measured ones.

(2) In RDR-FSW process, the tool pin with sub-size concave shoulder has dominant effect on the temperature field near the tool. Furthermore, the material flow velocity around the tool pin is confined to a relatively small region due to reverse rotating assisted shoulder. The region with the same velocity magnitude near the tool pin at the RS is larger than that at the AS since the bulk material flow by the tool pin is from RS.

(3) Within the range of the welding parameters used in this study, it could be found that the shape and size of TMAZ under the assisted shoulder are mainly affected by the rotating speed of the assisted shoulder, while the shape and size of TMAZ near the tool pin and under the sub-size concave shoulder are mainly influenced by both the rotating speed of the assisted shoulder and the tool pin. The welding speed has a slight impact on the shape and size of TMAZ. The symmetry of the TMAZ at AS and RS can be improved with an increase of the tool pin rotation speed.

References

1. Mishra RS, Ma ZY (2005) Friction stir welding and processing. Mater Sci Eng R 50(1–2):1–78
2. Nandan R, DebRoy T, Bhadeshia HKDH (2008) Recent advances in friction stir welding-process, weldment structure and properties. Progr Mater Sci 53:980–1023
3. Chen C, Kovacevic R (2004) Thermomechanical modeling and force analysis of friction stir welding by the finite element method. J Mech Eng Sci 218(5):509–519
4. Zimmer S, Langlois L, Laye J (2009) Experimental investigation of the influence of the FSW plunge processing parameters on the maximum generated force and torque. Int J Advan Manuf Technol 47(1–4):201–215
5. Li JQ, Liu HJ (2013) Effects of welding speed on microstructures and mechanical properties of AA2219-T6 welded by the reverse dual-rotation friction stir welding. Int J Advan Manuf Technol 68(9–12):2071–2083
6. Thomas WM, Norris IM, Staines DG, Watts ER (2005) Friction stir welding—process developments and variant techniques. The SME Summit 2005, Oconomowoc, Milwaukee, USA
7. Li JQ, Liu HJ (2013) Characteristics of the reverse dual-rotation friction stir welding conducted on 2219-T6 aluminum alloy. Mater Design 45:148–154
8. Shi L, Wu CS, Liu HJ (2014) Modeling the material flow and heat transfer in reverse dual-rotation friction stir welding. J Mater Eng Perform 23(8):2918–2929
9. Shi L, Wu CS, Liu HJ (2014) Numerical analysis of heat generation and temperature field in reverse dual-rotation friction stir welding. Int J Advan Manuf Technol 74(1–4):319–334
10. Nandan R, Roy GG, Lienert TJ, DebRoy T (2007) Three-dimensional heat and material flow during friction stir welding of mild steel. Acta Mater 55:883–895
11. Cho HH, Hong ST, Roh JH, Choi HS, Kang SH, Steel RJ, Han HN (2013) Three-dimensional numerical and experimental investigation on friction stir welding processes of ferritic stainless steel. Acta Mater 61:2649–2661
12. Wu CS, Zhang WB, Shi L, Chen MA (2012) Visualization and simulation of the plastic material flow in friction stir welding of aluminum alloy 2024 plates. Trans Nonferr Metal Soc China 22(6):1445–1451

13. Sheppard T, Jackson A (1997) Constitutive equations for use in pre-diction of flow stress during extrusion of aluminium alloys. Mater Sci Technol 13(3):203–209

14. Schmidt H, Dickerson TL, Hattel J (2006) Material flow in butt friction stir welds in AA2024-T3. Acta Mater 54:1199–1209

15. Awang M, Mucino VH, Feng Z, David SA (2005) Thermomechanical modeling of friction stir spot welding (FSSW) process: use of an explicit adaptive meshing scheme, Proceedings of the SAE 2005 World Congress & Exhibition, 2005 April 11–14

16. Mehta M, Chatterjee K, De A (2013) Monitoring torque and traverse force in friction stir welding from input electrical signatures of driving motors. Science and Technology of Welding and Joining 18(3): 191–197

17. Zhang Z, Xiao BL, Ma ZY (2014) Hardness recovery mechanism in the heat-affected zone during long-term natural aging and its influ-ence on the mechanical properties and fracture behavior of friction stir welded 2024Al–T351 joints. Acta Mater 73:227–239